

Efficient Quantum Gates for Individual Nuclear Spin Qubits by Indirect Control

Swathi S. Hegde, Jingfu Zhang, and Dieter Suter

Fakultät Physik, Technische Universität Dortmund, D-44221 Dortmund, Germany

Hybrid quantum registers, such as electron-nuclear spin systems, have emerged as promising hardware for implementing quantum information and computing protocols in scalable systems. Nevertheless, the coherent control of such systems still faces challenges. Particularly, the lower gyromagnetic ratios of the nuclear spins cause them to respond slowly to control fields, resulting in gate times that are generally longer than the coherence time of the electron. Here, we demonstrate a scheme for circumventing this problem by indirect control: we apply a small number of short pulses only to the electron and let the full system undergo free evolution under the hyperfine coupling between the pulses. Using this scheme, we realize robust quantum gates in an electron-nuclear spin system, including a Hadamard gate on the nuclear spin and a controlled-NOT gate with the nuclear spin as the target qubit. The durations of these gates are shorter than the electron coherence time, and thus additional operations to extend the system coherence time are not needed. Our demonstration serves as a proof of concept for achieving efficient coherent control of electron-nuclear spin systems, such as NV centers in diamond. Our scheme is still applicable when the nuclear spins are only weakly coupled to the electron.

Spin-based quantum registers have come up as a feasible architecture for implementing quantum computing [1, 2]. Among them are the hybrid systems consisting of electron and nuclear spins such as Nitrogen Vacancy (NV) centers in diamond [3–13]. Specific properties of their subsystems are the distinct gyromagnetic ratios, which result, e.g. in the requirement that the frequencies of the control fields applied to electronic and nuclear spins lie in the microwave (MW) and radiofrequency (RF) regimes respectively. The fast gate operation times on the electrons (order of ns) and the long coherence times of the nuclear spins (order of ms) serve as efficient control and memory channels. However, the lower gyromagnetic ratios of the nuclear spins result in longer nuclear spin gate operation times (a few tens of μs), which can exceed the electron coherence times ($\approx 1 - 25 \mu\text{s}$) at room temperature, thus posing a major challenge for coherent control of electron-nuclear spin systems. Techniques like dynamical decoupling (DD) can partly alleviate this issue by extending the coherence times of the electron [14–19], but the additional DD pulses increase the control cost.

Previously, one- and two-qubit operations were demonstrated using RF pulses on the nuclear spin that had strong hyperfine coupling of $\approx 130 \text{ MHz}$ [20–22]. Such strong couplings enhance the nuclear spin Rabi frequency allowing fast RF operations (order of ns) and hence direct control of nuclear spins was feasible [21, 23, 24]. However, scalable quantum computing requires coherent control of tens to hundreds of qubits and the control of dipolar coupled nuclear spins gets challenging with increasing distance from the electrons. To avoid these challenges, indirect control (IC) of the nuclear spins has also been incorporated [25–30]. In this approach, the control fields are applied only on the electron, combined with free evolution of the system under the hyperfine couplings. However, most of the earlier works based on IC required a large number of control operations, thereby increasing the control overhead [28, 31].

In this letter, we experimentally implement efficient

quantum gates in an NV center in diamond at room temperature, using IC with minimal control cost of only 2-3 of short MW pulses and delays. Our approach allows variable delays and pulse parameters. As such, it differs from earlier work [31] that used many DD cycles with fixed delays. We use this approach to demonstrate quantum gates that are required for a universal set of gates: a Hadamard gate on a nuclear spin, and a controlled-NOT (CNOT) gate with control on the electron and target on the nuclear spin.

We consider a single NV center that consists of a spin-1 electron coupled to a spin-1 ^{14}N and a spin-1/2 ^{13}C (see Supplemental Material [32]). We perform the operations on the electron and ^{13}C by focussing on a subspace of the system where the ^{14}N is in the $m_N = 1$ state. We then can write the secular part of the electron- ^{13}C Hamiltonian in the lab frame as $\mathcal{H}/(2\pi) = D(S_z^2 \otimes E_2) - (\nu_e - A_N)(S_z \otimes E_2) - \nu_C(E_3 \otimes I_z) + A_{zz}(S_z \otimes I_z) + A_{zx}(S_z \otimes I_x)$, where S_z and $I_{z/x}$ are the spin operators for electron and ^{13}C respectively, E_n is an $n \times n$ identity matrix, $D = 2.87 \text{ GHz}$ is the zero field splitting, $\nu_e = -414 \text{ MHz}$ and $\nu_C = 0.158 \text{ MHz}$ are the Larmor frequencies of the electron and ^{13}C in a 14.8 mT field, $A_N = -2.16 \text{ MHz}$ is the hyperfine coupling with ^{14}N and $A_{zz} = -0.152 \text{ MHz}$ and $A_{zx} = 0.110 \text{ MHz}$ are the hyperfine couplings with ^{13}C . The eigenstates of \mathcal{H} are $|0 \uparrow\rangle, |0 \downarrow\rangle, |-1\varphi_-\rangle, |-1\psi_-\rangle, |1\varphi_+\rangle, |1\psi_+\rangle$, where $\{|0\rangle, |\pm 1\rangle\}$ are the eigenstates of S_z , and

$$\begin{aligned} |\varphi_{\pm}\rangle &= \cos(\kappa_{\pm}/2)|\uparrow\rangle + \sin(\kappa_{\pm}/2)|\downarrow\rangle \\ |\psi_{\pm}\rangle &= -\sin(\kappa_{\pm}/2)|\uparrow\rangle + \cos(\kappa_{\pm}/2)|\downarrow\rangle. \end{aligned} \quad (1)$$

Here $\{|\uparrow\rangle, |\downarrow\rangle\}$ are the eigenstates of I_z , and $\kappa_{\pm} = \arctan[A_{zx}/(A_{zz} \mp \nu_C)]$ is the angle between the quantization axis of the ^{13}C and the NV axis.

We implement the quantum gates U_T in the $m_S = \{0, -1\}$ and $m_N = 1$ manifold and refer to it as the system subspace. This choice of subspace is realized by

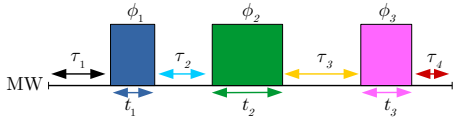


FIG. 1: MW pulse sequence to realize U_T by IC, at a fixed ω_1 . The delays τ_i , MW pulse durations t_i and phases ϕ_i are the free variables to be optimized.

using MW pulses with a Rabi frequency of ≈ 0.5 MHz ($\ll A_N$), which covers all electron spin resonance (ESR) transitions in the system subspace but leaves states untouched where the ^{14}N is in a different state. For the system subspace, the Hamiltonian is $\mathcal{H}_s/(2\pi) = |0\rangle\langle 0| \otimes \mathcal{H}_0 + |-1\rangle\langle -1| \otimes \mathcal{H}_{-1}$, where $\mathcal{H}_0 = -\nu_C I_z$ and $\mathcal{H}_{-1} = -(\nu_C + A_{zz})I_z - A_{zx}I_x$ are ^{13}C spin Hamiltonians when the electron is in $|0\rangle$ or $|-1\rangle$, respectively.

We implement two examples of U_T :

$$U_H = E_2 \otimes \begin{bmatrix} 1 & 1 \\ 1 & -1 \end{bmatrix} / \sqrt{2}$$

$$U_{CNOT} = |0\rangle\langle 0| \otimes E_2 + |-1\rangle\langle -1| \otimes e^{-i\pi I_x}. \quad (2)$$

The first is a Hadamard gate while the second is a CNOT gate, both targeting ^{13}C , in a basis defined in Ref. [33]. To check the implementation of U_T , we initialize the system into a pure state, apply U_T and then perform a partial tomography of the final state by recording free precession signals (FIDs).

For practical applications, it is useful to allow additional degrees of freedom, such as variable pulse rotation angles and finite pulse durations. These degrees of freedom allow us to compensate experimental errors via numerical optimization of the pulse sequence parameters. As shown in Fig. 1, we consider a pulse sequence consisting of delays τ_i and MW pulses with durations t_i and phases ϕ_i where $i = 1 \dots n$, n is the number of pulses. We fix the frequency of the pulses to be resonant with the ESR transition $0 \leftrightarrow -1$ and the Rabi frequency $\omega_1/2\pi$ to 0.5 MHz. During τ_i , the system freely evolves under \mathcal{H}_s such that $U_i^f = e^{-i\mathcal{H}_s\tau_i}$. The control Hamiltonians during the MW pulse segments are $\mathcal{H}_i^{MW} = \omega_1[\cos\phi_i(s_x \otimes E_2) + \sin\phi_i(s_y \otimes E_2)] + \mathcal{H}_s$, where $s_{x/y}$ denote the spin-1/2 operators for the electron, and the corresponding operators are $U_i^{MW} = e^{-i\mathcal{H}_i^{MW}t_i}$. The total propagator U is the time ordered product of U_i^f and U_i^{MW} . The overlap between U and U_T is defined by the fidelity $F = |\text{Tr}(U^\dagger U_T)|/4$. We maximize F numerically, using a MATLAB[®] subroutine implementing a genetic algorithm [34]. The solution returns the pulse sequence parameters t_i , τ_i and ϕ_i . The sequences were made robust against fluctuations of the MW pulse amplitude by optimizing F over a range $\omega_1/(2\pi) = [0.48, 0.52]$ MHz. Table I summarizes the optimized pulse parameters for U_H and U_{CNOT} , and the average gate fidelities are $> 96\%$ and $> 97\%$, respectively. The resulting trajectories of the electron and ^{13}C on the Bloch-sphere is shown in the Supplemental Material [32].

TABLE I: MW pulse sequence parameters for U_H and U_{CNOT} . The time durations and phases are in units of μs and radians, respectively.

	τ_1	τ_2	τ_3	τ_4	t_1	t_2	t_3	ϕ_1	ϕ_2	ϕ_3
U_H	0.74	0.22	0.43	0.89	0.23	1.26	1.50	$3\pi/2$	$3\pi/2$	$\pi/2$
U_{CNOT}	3.78	2.11	2.15	0.63	1.88	3.96	1.90	0	$\pi/5$	$\pi/2$

Our experiments started with an initial laser pulse with a wavelength of 532 nm, a duration of 5 μs , and a power of ≈ 0.5 mW which initialized the electron to $|0\rangle$ but left the ^{13}C in a mixed state. To initialize ^{13}C to $|\uparrow\rangle$, we resorted to the IC method [32, 35, 36]. Starting from $\psi_0 = |0\uparrow\rangle$, we implemented the circuits shown in Figs. (2, 3). Depending on the experiment, we either observed the electron or the ^{13}C state via FID measurements. The readout process consisted of another laser pulse with the same wavelength and 400 ns duration and was used to measure the population of $m_S = 0$.

Figure 2(a) shows the pulse sequence for implementing and detecting the effect of U_H . The first U_H generates $|0\rangle \otimes (|\uparrow\rangle + |\downarrow\rangle)/\sqrt{2}$. The ^{13}C coherence is then allowed to evolve for a variable time t after which we apply another U_H to convert one component of the coherence to population. Lastly, a clean-up operation, with MW pulse sequence ($90_x - \tau_c - 90_y$), where $90_{x/y}$ are pulses with rotation angle 90° about the x/y -axis applied to the $m_S = 0 \leftrightarrow 1$ transition with 0.5 MHz Rabi frequency and $\tau_c = 1/(2|A_{zz}|)$ is the delay, represented by the dotted box transfers the population from $|0\downarrow\rangle$ to $|1\downarrow\rangle$. The final read-out operation thus detects only the population of $|0\uparrow\rangle$, which depends on t as $[1 + \cos(2\pi\nu_C t)]/2$. In the frequency domain, this corresponds to a peak at ν_C .

Using the pulse sequence in Fig. 2(a), we performed two

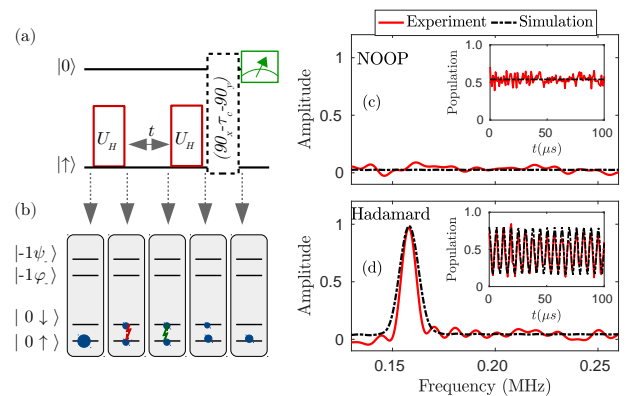


FIG. 2: (a) Quantum circuit to test U_H . The MW pulse sequence parameters for U_H are given in Table I. The clean-up operation is represented by the dotted box. (b) Populations (solid circles) and coherences (zig-zag arrows) at each stage of the pulse sequence in (a). (c, d) ^{13}C spin spectra obtained by the pulse sequence in (a). (c) Without the first U_H . (d) With both U_H . Inset: Final population of $|0\uparrow\rangle$ as a function of t .

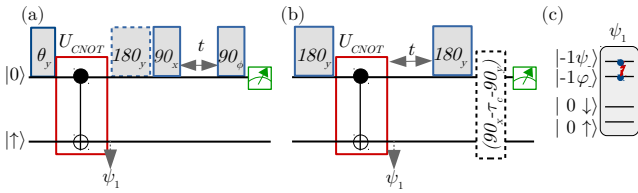


FIG. 3: Quantum circuits to test U_{CNOT} . The MW pulse sequence parameters for U_{CNOT} indicated by red empty boxes are given in Table. I. $\theta_{x/y/\phi}$ denote operations with rotation angles θ about the $x/y/\phi$ axes that are resonant with the transition $0 \leftrightarrow -1$ and with Rabi frequencies of 8 MHz. (a) Pulse sequence to demonstrate the effect of U_{CNOT} on different input states via electron spin detection. ϕ is the detuning phase. In the presence (absence) of the 180_y operation indicated by the dashed box, the FID measurement is used to determine the population of the $m_S = -1$ ($m_S = 0$) after U_{CNOT} . (b) Pulse sequence to demonstrate the effect of U_{CNOT} via ^{13}C spin detection. (c) Pictorial representation of state ψ_1 .

experiments to compare the effect of U_H : (1) without the first U_H (i.e., no operation, also known as NOOP) and (2) with both U_H . In the case of NOOP, the system was in ψ_0 during the free evolution period. Since ψ_0 does not contain ^{13}C coherence the resulting frequency domain signal does not contain a resonance at ν_C , as shown in Fig. 2(c). With both U_H present, we observe in Fig. 2(d) a resonance peak at ν_C as expected. We numerically simulated the pulse sequence in Fig. 2(a) without and with the first U_H , and then calculated the final populations of $|0\uparrow\rangle$ as a function of t . To match the theoretical signal with the experimental one, we had to scale it by a factor 0.9 for NOOP and 0.8 for U_H (i.e., with two U_H), and estimated the infidelity of the experimental U_H as $\approx 10\%$.

The schemes to demonstrate U_{CNOT} are shown in Fig. 3. Using the pulse sequence in Fig. 3(a), we demonstrated the effect of U_{CNOT} in $m_S = -1$ by measuring electron spin spectra. Choosing for the flip-angle θ of the initial θ_y operation [37, 38] a value of π , we exchanged the populations of the $|0\uparrow\rangle \leftrightarrow |-1\uparrow\rangle \approx |-1\rangle \otimes (|\phi_-\rangle - |\psi_-\rangle)/\sqrt{2}$ according to Eq. (1). The subsequent U_{CNOT} transformed $|-1\uparrow\rangle$ to $-i|-1\downarrow\rangle \approx -i|-1\rangle \otimes (|\phi_-\rangle + |\psi_-\rangle)/\sqrt{2}$, since by definition of Eq. (2), U_{CNOT} flips the ^{13}C state when the electron is in $|-1\rangle$. To measure the state after U_{CNOT} , we transferred the population of $|-1\downarrow\rangle$ to $|0\downarrow\rangle$ using a hard 180_y operation. The readout process, which measures the population of $m_S = 0$, can then be used to determine the population left in $|-1\downarrow\rangle$ by U_{CNOT} . The sequence $(90_x - t - 90_\phi)$ in Fig. 3(a) implements the electron spin FID measurement, where the 90_x pulse creates electron coherence and the 90_ϕ pulse converts one component of the evolved coherence to population [6, 36]. Here we incremented the phase $\phi(t) = -2\pi\nu_d t$ linearly with t , using a detuning frequency ν_d of 3 MHz. We then measured the population of $m_S = 0$ with the readout laser pulse as a function of t and its Fourier transform

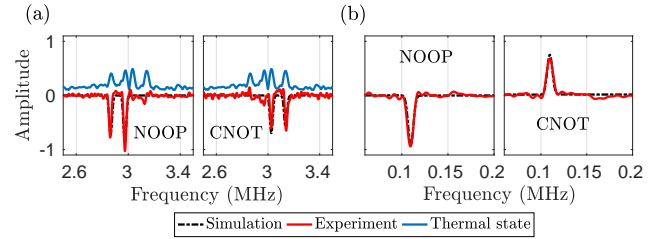


FIG. 4: (a) Electron spin spectra for the pulse sequence corresponding to Fig. 3(a) without and with U_{CNOT} where $\theta_y = \pi$. The thermal state spectra on top are shifted vertically for reference. The electron spin spectra are centered around the detuning frequency 3 MHz. (b) ^{13}C spin spectra obtained by the pulse sequence shown in Fig. 3(b) without and with U_{CNOT} . The peaks appear at $\nu_- = 0.11$ MHz.

gives the frequency domain signal. Thus, as seen in the electron spin spectra in Fig. 4(a), the change of nuclear spin state resulted in a different frequency of the ESR lines in the case of U_{CNOT} as compared to NOOP.

Since U_{CNOT} targets the ^{13}C , we also observed its effects on the ^{13}C by measuring the nuclear spin spectra using the pulse sequence in Fig. 3(b). The initial 180_y operation transforms $|0\uparrow\rangle$ to $|-1\uparrow\rangle \approx |-1\rangle \otimes (|\phi_-\rangle - |\psi_-\rangle)/\sqrt{2}$. After implementing U_{CNOT} , we allowed the ^{13}C coherence between states $|\phi_-\rangle$ and $|\psi_-\rangle$ to evolve for a variable time t , as shown in Fig. 3(c), and then applied another 180_y operation to the electron to bring the evolved state from $m_S = -1$ to $m_S = 0$. The subsequent clean-up operation removed the population of $|0\downarrow\rangle$ and allowed us to measure the remaining population of $|0\uparrow\rangle$ with the readout laser pulse. The experimental ^{13}C spectra without and with U_{CNOT} are shown in Fig. 4(b). The resonance frequency of the peak at 0.11 MHz agree with the expected resonance frequency ν_- of the ^{13}C for $m_S = -1$. Comparing with NOOP, the inverted amplitude shows that U_{CNOT} flipped the ^{13}C states in $m_S = -1$. In Figs. 4(a, b), we show the matching simulations, calculated for ideal pulses, scaled by a factor 0.8.

As an additional test of the sequence for different input states, we first applied a selective rotation, when $m_N = 1$ [39], of ψ_0 by an angle θ_y to generate the superposition state $\psi_\theta = \cos(\theta/2)|0\uparrow\rangle + \sin(\theta/2)|-1\uparrow\rangle$. As shown in Fig. 3(a), we then applied either a NOOP or U_{CNOT} . The latter transforms ψ_θ to $\cos(\theta/2)|0\uparrow\rangle - i\sin(\theta/2)|-1\downarrow\rangle$, which is entangled for $\theta \neq n\pi$ with integer n . Ideally, the amplitude of the resonance line for the transition $|0\downarrow\rangle \leftrightarrow |1\downarrow\rangle$ [40] is proportional to the population $P_{0\downarrow}$. We thus determined $P_{0\downarrow}$ and the results, which are shown in Fig. 5, demonstrate the effect of U_{CNOT} for the 2 cases where the control qubit is $|0\rangle$ or $|-1\rangle$. Figure 5(a) shows $P_{0\downarrow}$ after applying NOOP or U_{CNOT} to ψ_θ , as a function of θ in the absence of the 180_y operation indicated by the dotted box in Fig. 3(a). This pulse sequence allows us to measure the effect of U_{CNOT} when the electron spin is $|0\rangle$. The curves for both cases are similar since U_{CNOT} does not change the ^{13}C state when the electron spin is

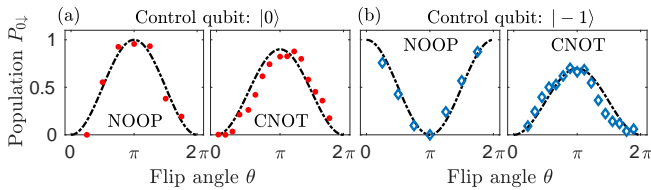


FIG. 5: $P_{0\downarrow}$ as a function of θ corresponding to the pulse sequences shown in Fig. 3(a). The diamonds and solid circles are the experimental data, and the dashed lines are the matching simulations.

$|0\rangle$. In Fig. 5(b) we show the effect of U_{CNOT} when the electron spin is $|-1\rangle$. To read out the population of $|-1\rangle$, we first applied a 180_y operation, as shown in Fig. 3(a) and then measured the electron spin FID in $m_S = \{0, 1\}$. In this case, the $P_{0\downarrow}$ vs θ curve flipped for U_{CNOT} compared to NOOP, indicating the change of the ^{13}C state when the electron is in $|-1\rangle$. By fitting the experimental $P_{0\downarrow}$ with the corresponding theoretical populations for various θ as shown in Fig. 5, we estimated the experimental infidelity due to U_{CNOT} as 20% [32]. *Discussion.*— Our experiments convincingly show that the IC scheme is a very effective approach to implement operations in systems consisting of 3 types of qubits. The advantages of this approach will become even more important as the number of qubits increases. While a full implementation of the approach in large quantum registers is beyond the scope of this paper, we have tested the basic scheme through numerical simulations of gates in multiqubit systems with up to six qubits. The simulations show that the procedure scales relatively favorably with the size of the system [32]. For the 6-qubit system our method to control individual ^{13}C spins was efficient as it required 3-4 MW pulses and the total duration was $< 30 \mu\text{s}$. The theory [25, 41] regarding the bounds for the control overhead and the condition to retain efficiency for larger spin systems is explained in [32].

Conclusion.— We experimentally demonstrated full coherent control i.e., state initialization, gate implementa-

tion and detection of the electron-nuclear spin system in the NV center of diamond using the methods of IC. We specifically chose a center with a small hyperfine coupling, some three orders of magnitude weaker than that of the nearest neighbor ^{13}C spins. The distance between the electron and ^{13}C is $\approx 0.89 \text{ nm}$ [32]. These remote spins are much more abundant than the nearest neighbors and their relaxation times much longer. However, since their coupling to RF fields is also much weaker, direct RF excitation does not lead to efficient control operations. The IC techniques that we have demonstrated allow much faster controls and therefore overall higher fidelity - an essential prerequisite for scalable quantum systems. Specifically, we have implemented a Hadamard gate on ^{13}C and a CNOT gate, where the electron is the control qubit and ^{13}C the target qubit, using only a small number of MW pulses and delays. The above gate operations targeted the subspace $m_S = \{0, -1\}$ and $m_N = 1$. If we consider the control state of the ^{14}N , i.e. $m_N = 1$, in the whole space with $m_N = \{0, -1, 1\}$, then our U_{CNOT} is a Toffoli gate in 12 dimensions. Since the total duration of the pulse sequence was well within the electron coherence time ($T_2^* \approx 20 \mu\text{s}$), additional coherence preserving control operations were not required. However, for complex algorithms consisting of many gates, it may be necessary to include DD. While we have implemented this scheme in the diamond NV center at room temperature in a small external magnetic field, it remains applicable over a much wider parameter range and can clearly be adapted to other quantum systems, thus opening the ways for many different implementations of advanced quantum algorithms using indirect control schemes.

This work was supported by the DFG through grants SU 192/34-1 and SU 192/31-1 and by the European Union's Horizon 2020 research and innovation programme under grant agreement No 828946. The publication reflects the opinion of the authors; the agency and the commission may not be held responsible for the information contained in it. SH thanks Dr T S Mahesh for fruitful discussions on genetic algorithms.

-
- [1] M. A. Nielsen and I. Chuang, *Quantum computation and quantum information* (Cambridge University Press, Cambridge, England, 2002).
 - [2] J. Stolze and D. Suter, *Quantum computing: a short course from theory to experiment* (John Wiley & Sons, Berlin, 2008).
 - [3] T. Gaebel, M. Domhan, I. Popa, C. Wittmann, P. Neumann, F. Jelezko, J. R. Rabreau, N. Stavrias, A. D. Greentree, S. Praver, et al., *Nature Physics* **2**, 408 (2006).
 - [4] P. Neumann, N. Mizuochi, F. Rempp, P. Hemmer, H. Watanabe, S. Yamasaki, V. Jacques, T. Gaebel, F. Jelezko, and J. Wrachtrup, *science* **320**, 1326 (2008).
 - [5] J. Wrachtrup, S. Y. Kilin, and A. Nizovtsev, *Optics and Spectroscopy* **91**, 429 (2001).
 - [6] D. Suter and F. Jelezko, *Progress in nuclear magnetic resonance spectroscopy* **98**, 50 (2017).
 - [7] L. Childress, M. G. Dutt, J. Taylor, A. Zibrov, F. Jelezko, J. Wrachtrup, P. Hemmer, and M. Lukin, *Science* **314**, 281 (2006).
 - [8] G. Fuchs, V. Dobrovitski, D. Toyli, F. Heremans, and D. Awschalom, *Science* **326**, 1520 (2009).
 - [9] G. Balasubramanian, P. Neumann, D. Twitchen, M. Markham, R. Kolesov, N. Mizuochi, J. Isoya, J. Achard, J. Beck, J. Tissler, et al., *Nature materials* **8**, 383 (2009).
 - [10] P. C. Maurer, G. Kucsko, C. Latta, L. Jiang, N. Y. Yao, S. D. Bennett, F. Pastawski, D. Hunger, N. Chisholm, M. Markham, et al., *Science* **336**, 1283 (2012).
 - [11] E. Herbschleb, H. Kato, Y. Maruyama, T. Danjo,

- T. Makino, S. Yamasaki, I. Ohki, K. Hayashi, H. Morishita, M. Fujiwara, et al., *Nature communications* **10**, 3766 (2019).
- [12] C. Bradley, J. Randall, M. Abobeih, R. Berrevoets, M. Degen, M. Bakker, M. Markham, D. Twitchen, and T. Taminiau, *Physical Review X* **9**, 031045 (2019).
- [13] A. Gali, M. Fyta, and E. Kaxiras, *Physical Review B* **77**, 155206 (2008).
- [14] S. Meiboom and D. Gill, *Review of scientific instruments* **29**, 688 (1958).
- [15] G. S. Uhrig, *Physical Review Letters* **98**, 100504 (2007).
- [16] J. Zhang and D. Suter, *Physical review letters* **115**, 110502 (2015).
- [17] T. Van der Sar, Z. Wang, M. Blok, H. Bernien, T. Taminiau, D. Toyli, D. Lidar, D. Awschalom, R. Hanson, and V. Dobrovitski, *Nature* **484**, 82 (2012).
- [18] D. Suter and G. A. Álvarez, *Rev. Mod. Phys.* **88**, 041001 (2016), URL <http://link.aps.org/doi/10.1103/RevModPhys.88.041001>.
- [19] J. Zhang, A. M. Souza, F. D. Brandao, and D. Suter, *Physical review letters* **112**, 050502 (2014).
- [20] F. Jelezko, T. Gaebel, I. Popa, M. Domhan, A. Gruber, and J. Wrachtrup, *Physical Review Letters* **93**, 130501 (2004).
- [21] J. Shim, I. Niemeyer, J. Zhang, and D. Suter, *Physical Review A* **87**, 012301 (2013).
- [22] K. R. K. Rao and D. Suter, *Physical Review B* **94**, 060101 (2016).
- [23] J. Maze, J. Taylor, and M. Lukin, *Physical Review B* **78**, 094303 (2008).
- [24] P. Cappellaro, L. Jiang, J. Hodges, and M. D. Lukin, *Physical review letters* **102**, 210502 (2009).
- [25] N. Khaneja, *Physical Review A* **76**, 032326 (2007).
- [26] F. Wang, Y.-Y. Huang, Z.-Y. Zhang, C. Zu, P.-Y. Hou, X.-X. Yuan, W.-B. Wang, W.-G. Zhang, L. He, X.-Y. Chang, et al., *Physical Review B* **96**, 134314 (2017).
- [27] Y. Zhang, C. A. Ryan, R. Laflamme, and J. Baugh, *Physical review letters* **107**, 170503 (2011).
- [28] J. S. Hodges, J. C. Yang, C. Ramanathan, and D. G. Cory, *Physical Review A* **78**, 010303 (2008).
- [29] T. Taminiau, J. Wagenaar, T. Van der Sar, F. Jelezko, V. V. Dobrovitski, and R. Hanson, *Physical review letters* **109**, 137602 (2012).
- [30] C. D. Aiello and P. Cappellaro, *Physical Review A* **91**, 042340 (2015).
- [31] T. H. Taminiau, J. Cramer, T. van der Sar, V. V. Dobrovitski, and R. Hanson, *Nature nanotechnology* **9**, 171 (2014).
- [32] See the Supplemental Material for details of NV center system, Bloch Sphere representation of the gates, initial state determination, error estimation for CNOT, gates in multiqubit systems, spatial distance between the electron and the ^{13}C , effects of operations on the ^{14}N used in this work, which includes Refs. [38, 41–44].
- [33] These operations are written in the computational basis states $\{|0 \uparrow\rangle, |0 \downarrow\rangle, |-1 \uparrow\rangle, |-1 \downarrow\rangle\}$ which is related to the energy eigenbasis by a transformation matrix $V = |0\rangle\langle 0| \otimes E_2 + |-1\rangle\langle -1| \otimes e^{-i\kappa - I_y}$.
- [34] M. Mitchell, *An Introduction to Genetic Algorithms* (MIT Press, Cambridge, MA, USA, 1998), ISBN 0262631857.
- [35] J. Zhang, S. S. Hegde, and D. Suter, *Physical Review Applied* **12**, 064047 (2019).
- [36] J. Zhang, S. S. Hegde, and D. Suter, *Physical Review A* **98**, 042302 (2018).
- [37] Here the hard θ_y operation refers to the operation in subspace $m_S = \{0, -1\}$ and $m_N = \{0, -1, 1\}$. The corresponding Rabi frequency is 8MHz.
- [38] J. Cavanagh, W. J. Fairbrother, A. G. Palmer III, and N. J. Skelton, *Protein NMR spectroscopy: principles and practice* (Elsevier, 1995).
- [39] If θ_y operation is a hard pulse as before, then for any value of θ not equal to integral multiple of π , this pulse creates electron spin coherence in $m_N = \{0, -1, 1\}$ subspaces that evolve during the gate operations implemented in the system subspace. For simplicity, we here chose θ_y operation as selective pulse subjected to $m_N = 1$ with Rabi frequency 0.5 MHz as we vary θ value.
- [40] Unlike the 4 ESR peaks in $m_S = \{0, -1\}$ subspace, the ESR spectra in $m_S = \{0, 1\}$ subspace has only two observable resonance peaks, where one peak corresponds to total population of state $|\uparrow\rangle$ and the other peak corresponds to total population of state $|\downarrow\rangle$ [see Ref. 32].
- [41] F. Lowenthal, *The Rocky Mountain Journal of Mathematics* **1**, 575 (1971).
- [42] L. Jiang, J. M. Taylor, A. S. Sørensen, and M. D. Lukin, *Physical Review A* **76**, 062323 (2007).
- [43] J. Zhang, S. Saha, and D. Suter, *Physical Review A* **98**, 052354 (2018).
- [44] N. Mizuochi, P. Neumann, F. Rempp, J. Beck, V. Jacques, P. Siyushev, K. Nakamura, D. Twitchen, H. Watanabe, S. Yamasaki, et al., *Physical review B* **80**, 041201 (2009).